Development and testing of the gravitational wave antenna MiniGRAIL in its full-featured configuration

Usenko, O.

Chapter 4

First calibration run of MiniGRAIL

Introduction

Because we have modified so many components of the system, as we described in the previous chapter, and due to the limited budget for liquid helium, we decided to do a short run aimed at testing a modified setup and verifying a calibration procedure we have developed. In this chapter we report the results of the calibration run of MiniGRAIL we performed in autumn 2010. For the first time we started the run with all 6 transducers mounted on the sphere. Each transducer was coupled to two stage DC SQUID amplifier. Five 2-stage SQUID modules consisted of commercial Quantum Design DC SQUID and custom design flux transformer SQUID for the second stage(see chapter 3). One module was a standard 2-stage Quantum Design module similar to the one used in Auriga experiment [66]. The parameters of transducers and impedance matching transformers are summarized in table 4.1

We have also mounted 7 mass-loaded PZT resonators(calibrators) for calibration purposes. Six calibrators are placed at the same polar angles as transducers but shifted by 60^o in azimuthal angles. The seventh calibrator is placed at an arbitrary position and is used to verify the direction reconstruction algorithms. The picture of the sphere with transducers and calibrators mounted is shown on figure 1.10 in chapter 1.

During the run we have cooled the system down to a temperature of $\approx 1\,K$. Unfortunately, due to a failure of some the switches and transducers only transducers at position 4 and 6 were operable, so we could not conduct the complete calibration procedure as planned. However we believe that we were able to extract some useful information which we will discuss further in this chapter.

Transducer position	1	2	3	4	5	6
Transducer capacitance* [nF]	3.9	3.0	4.9	3.4	4.5	4.6
Max V_{bias}, [V]	240	195	200	200	180	180
V_{bias} at $77\,K$, [V]	138	155	152	160	164	155
Transformer box	Tr1	Tr2	Tr3	Tr4	Tr5	Tr6
Primary Inductance, [H]	0.18	0.12	0.183	0.166	0.205	0.178
Secondary Inductance, [uH]	7	≈ 2	2.04	1.8	1.67	1.85
Coupling	0.49	0.85	0.85	0.6	0.86	0.84
SQUID gain, [$V/\Phi 0$]	0.16	0.16	0.13	0.79	0.18	0.16
Electric mode Q	-	-	-	-	6.3×10^4	6×10^4
Calibration mutual inductance, [nH]	300	128	n.a.	3	n.a.	n.a.
Decoupling Capacitor, [nF]	138.8	152.0	133.9	156.2	159.8	149.8

* measured at room temperature

Table 4.1**:** Properties of transducers and superconducting matching transformers

4.1 MiniGRAIL directional sensitivity with non-optimal transducer configuration

The first question we would like to answer is: how much does our experiment suffer from the reduction of the number of transducers?

In the case of an ideal sphere with degenerate quadrupole modes this would result a disastrous drop in directional sensitivity leaving the detector almost blind to some directions. However, on the real sphere the modes are split in frequency, so instead of being sensitive to the sum of modes amplitudes, defined by the sum of spherical harmonics at transducer position, the transducer sees each mode individually.

The force F_c applied by a calibrator to the sphere surface at position (ϕ_c, θ_c) will excite five quadrupolar modes of the sphere with amplitudes

$$\mathbf{a}_m(t) \propto \mathbf{Y}_m(\phi_c, \theta_c) F_c(t). \tag{4.1}$$

If the modes are degenerate, then for a set of J transducers the radial displacement $\mathbf{q}_j$ of a sphere surface at transducer position(ϕ_j,θ_j)is given by (see section 1.1.2 in chapter 1)

$$\mathbf{q}_j(t) = \alpha \mathbf{B}_{mj} \mathbf{a_m}(t) \tag{4.2}$$

By varying ϕ_c and θ_c we can map the sphere surface in terms of sensitivity of each transducer. Since all modes have the same frequency, we can expect that for some directions the amplitudes of the modes at the transducer j position might cancel each other. The resulting amplitude q_j would be very low, meaning that this particular transducer is not sensitive to that direction. We express the total direction sensitivity as root mean square of transducers sensitivities:

$$Q(\phi_c, \theta_c) = \sqrt{\frac{\sum_j \mathbf{q}_j^2}{J}}. \tag{4.3}$$

For six transducers in MiniGRAIL arrangement the direction sensitivity is almost uniform (figure 4.1(a)). If we only take into account transducers 4 and 6, the averaging will produce a complicated pattern, with sensitivity dropping by more than an order of magnitude in some directions(figure 4.1(b))

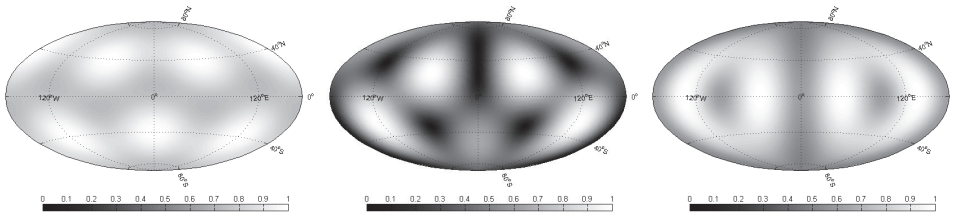

(a) (b) (c)

Figure 4.1**:** Directional sensitivity for full six(a) and for transducers #4 and #6 configuration for degenerate(b) and splitted(c) modes

If the modes are not degenerate then each transducer displacement amplitude q_j is split into a vector of five amplitudes $\mathbf{q}_{jm}$, which have different frequency and are seen by transducer independently. Again by doing an RMS averaging over m and then over j we can build the sensitivity map. The resulting pattern is much smoother, with the sensitivity only varying by about 50% (figure 4.1(c)). Another advantage of the non-degenerate modes is that each transducer has the information about all five quadrupole modes. In theory this allows direction reconstruction with less than five transducers. We will discuss it again in section 4.3.

In the analysis above we used a radial displacement of the sphere surface at the transducer position as the measure of sensitivity which is only valid for a wide band transducer like a piezo. It also does not take into account the noise which might significantly reduce the mode SNR. So real directional sensitivity degradation might be more significant.

4.2 Calibration

Here we describe the calibration procedure, we use to estimate the strain sensitivity of MiniGRAIL. First with the calibration transformer we do the energy calibration to measure the conversion factor between the energy stored in the mode and the current density at the SQUID input. Then we estimate the calibrators efficiency - by applying a known voltage to the calibrators we measure the energy deposited in the

modes. These two calibrations allow us to build the transfer function of the system and calculate the strain sensitivity of MiniGRAIL.

4.2.1 Energy calibration

Since in this run we have implemented calibration transformers, we do not need to use an extra calibrator as reported in [25], and are able to calibrate the read-out sensitivity directly. For better understanding it would be useful to show again a simplified version of capacitive transducer read out scheme on figure 4.2

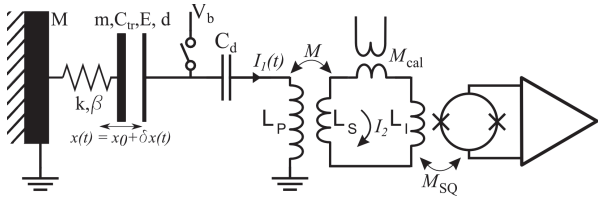

Figure 4.2**:** Capacitive transducer read-out scheme

If a charged transducer is excited from its equilibrium x_0, its position changes as $x(t) = x_0 + \delta x(t)$. The capacitance and the charge also changes as

$$\begin{cases} q(t) = q_0 + \delta q(t) \\ C_{tr}(t) = C_0 + \delta C_{tr}(t) \end{cases} \tag{4.4}$$

From the electrical point of view the transducer is just a parallel plate capacitor so the force between the electrode and the resonator is

$$F(t) = \frac{Eq}{2} \equiv \frac{q^2}{2\varepsilon_0 A} = \frac{1}{2\varepsilon_0 A}(q_0^2 + 2q_0\delta q(t) + \delta q^2(t)) \approx \frac{q_0^2}{2\varepsilon_0 A} + \frac{q_0 \delta q(t)}{2\varepsilon_0 A}. \tag{4.5}$$

From the mechanical point of view the transducer is a harmonic oscillator driven by a force F. We can write down the equation of motion of transducer

$$m(\delta x''(t) + \beta \delta x'(t) + k\delta x) = F(t), \tag{4.6}$$

A standard solution in frequency domain is the Lorentzian shape

$$\begin{aligned} &\delta x(-\omega^2 + \frac{i\omega\omega_0}{Q} + \omega_0^2) = \frac{F(\omega)}{m}, \\ &\delta x = \frac{E\delta q(\omega)}{m(-\omega^2 + \frac{i\omega\omega_0}{Q} + \omega_0^2)} \end{aligned} \tag{4.7}$$

We can also write the expression for voltage across the transducer

$$V(t) = \frac{q(t)}{C(t)} = \frac{q_0 + \delta q(t)}{C_0 + \delta C(t)} \approx \frac{q_0}{C_0} - \frac{q_0 \delta C}{C_0^2} + \frac{\delta q}{C_0} = V_0 + \frac{\delta q}{C_0}(1 - \frac{q_0 \delta C}{C_0 \delta q}) \tag{4.8}$$

given that $\frac{\delta C}{C_0} = -\frac{\delta d}{d_0} = \frac{\delta x}{d_0}$ and $\frac{q_0}{d_0} = E_0$, where d is the transducer gap, we get the final expression for the voltage

$$V(t) = V_0 + \frac{\delta q}{C_0}(1 - C_0 E_0 \delta x(t)) \tag{4.9}$$

Considering the harmonic calibration current $I(t) = I_0 exp(i\omega t)$ and combining equations 4.7 and 4.9 we can write the expression for the transducer impedance

$$Z_{tr}(\omega) = \frac{1}{i\omega C_0}(1 - \frac{E_0^2 C_0}{m} \frac{1}{-\omega^2 + \frac{i\omega\omega_0}{Q} + \omega_0^2}) \equiv \frac{1}{i\omega C_0} \frac{-\omega^2 + \frac{i\omega\omega_0}{Q} + \omega_0^2 - \frac{E_0^2 C_0}{m}}{-\omega^2 + \frac{i\omega\omega_0}{Q} + \omega_0^2} \tag{4.10}$$

The expression $\frac{E_0^2 C_0}{m}$ has a dimension of $[Hz^2]$ and is a resonance frequency shift due to electric field in a transducer. A new resonance frequency is ${\omega'_0}^2 = \omega_0^2 - \frac{E_0^2 C_0}{m}$. We define a coupling factor β^2 a the relative change in resonant frequency

$$\beta^2 = \frac{\omega_0^2 - {\omega'_0}^2}{\omega_0^2} \equiv \frac{E_0^2 C_0}{m \omega_0^2} \tag{4.11}$$

The final expression for transducer impedance including the coupling becomes

$$Z_{tr}(\omega) = \frac{1}{i\omega C_0} \frac{-\omega^2 + i\frac{\omega\omega_0}{Q} + \omega_0^2(1 - \beta^2)}{-\omega^2 + i\frac{\omega\omega_0}{Q} + \omega_0^2} \tag{4.12}$$

It can be shown that the function above has two resonance frequencies(corresponding to $\mathrm{Im}(Z(w)) = 0$) where impedance is at it's minimum ω_{res} and maximum ω_{ares} with the ratio of $\frac{\omega_{ares}^2}{\omega_{res}^2} = 1 - \beta^2$. If we generate a constant flux $\Phi_{cal}(\omega) = const$ with the calibration coil, the current generated in the primary and secondary loops of a matching transformer is

$$\begin{cases} I_2(\omega) = \frac{(\Phi_{cal} + I_1(\omega)M)}{L_2} \\ I_1(\omega) = \frac{i\omega M I_2(\omega)}{Z_1(\omega)}, \end{cases} \tag{4.13}$$

where $L_2 = L_s + L_i$ is the total inductance of the secondary loop and $Z_1(\omega) = Z_{tr}(\omega) + i\omega L_p$ is the impedance of the primary loop. We have neglected the impedance of the decoupling capacitor as it is much smaller then the impedance of the transducer and the primary coil. By combining both equations we get an expression for the current through the input coil of the SQUID

$$I_2(\omega) = \frac{\Phi_{cal}}{\left(L_2 - \frac{i\omega M^2}{Z_1(\omega)}\right)} = \frac{i\omega\Phi_{cal}}{i\omega L_2 + \frac{\omega^2 M^2}{Z_1(\omega)}} \equiv \frac{V_{cal}}{Z_m(\omega)}, \tag{4.14}$$

where Z_m is the impedance of the measurement circuit as seen from the SQUID input.

It can be shown that the frequency dependence of admittance $Y_m(\omega) = 1/Z_m(\omega)$ can be described by a curve similar to equation (4.12)

$$Y_m(\omega) = A\frac{-\omega^2 + i\frac{\omega\omega_0}{Q} + \omega_0^2(1-\beta'^2)}{-\omega^2 + i\frac{\omega\omega_0}{Q} + \omega_0^2}, \tag{4.15}$$

We note that the coupling factor β'^2 is different form the one in equation (4.12). From equations (4.14) and (4.15) we see that for $\omega \ll \omega_0$, $Y_m \approx 1/i\omega L_2 \approx A(1-\beta^2)$. Given that β^2 is typically in the order of $10^{-6} - 10^{-5}$ we get the expression for A

$$A = \frac{1}{i\omega L_2} \tag{4.16}$$

By sweeping the frequency of the calibration signal and fitting the measured current in the input coil of the SQUID with the equation (4.15) we can measure the equivalent impedance of all modes. As an example, the calibration curves of three most coupled modes for transducer 6 are shown on figure 4.3.

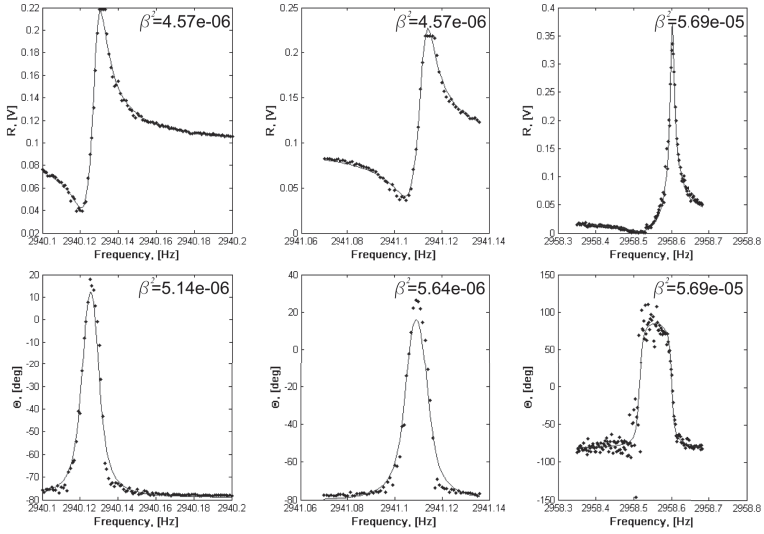

Figure 4.3**:** Calibration curves of the three most coupled modes

If the modes are only excited by the thermal noise, the current power spectral density around each resonant mode is [65, 67]

$$S_{I,m} = 4k_B T \frac{Q_a}{Q} \operatorname{Re}\left(Y_m(\omega)\right) + S_{vv}(\omega)|Y_m(\omega)|^2 + S_{ii}(\omega) + 2\operatorname{Re}\left(S_{iv}(\omega)Y_m^*(\omega)\right), \quad (4.17)$$

where S_{vv} and S_{ii} are the power spectral densities of the back-action and additive noise of the SQUID amplifier. S_{iv} is the cross-correlation between these terms. $\frac{Q_a}{Q}$ is the ratio between the measured quality factor, affected by cold damping, and the intrinsic quality factor of the mode.

The contribution of different noise terms to a total noise power spectral density is shown on figure 4.4. The circuit parameters match the design parameters of MiniGRAIL read-out. The resonator and the SQUID temperatures are set to $100\,mK$ and $350\,mK$ respectively.

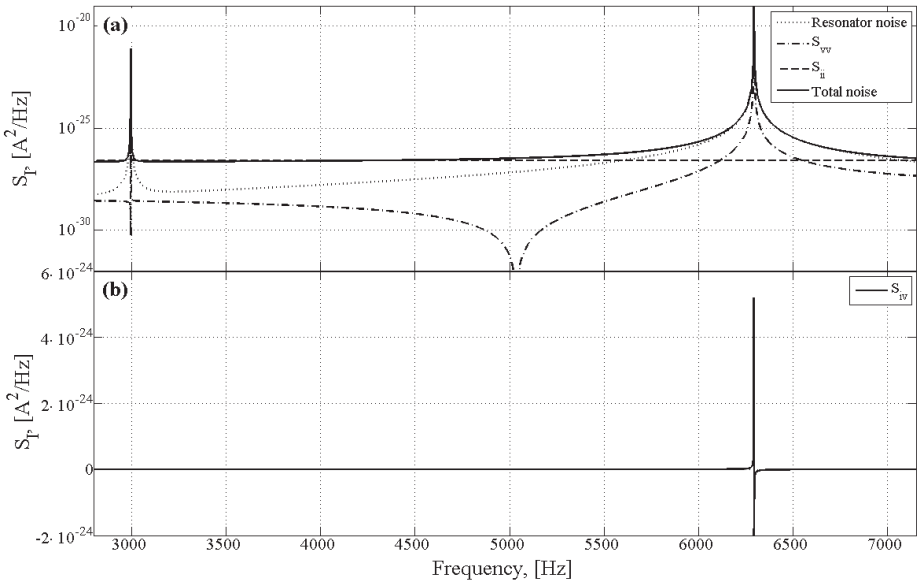

Figure 4.4**:** Current noise power spectral density at the SQUID input. The curves show the relative contribution of different noise terms from equation (4.17). The circuit parameters match the design parameters of MiniGRAIL read-out. The resonator and the SQUID temperatures are set to $100\,mK$ and $350\,mK$ respectively.

As we can see from the graph, close to the mechanical resonance the contributions of S_{vv}, S_{ii} and S_{iv} terms are small compared to the thermal noise of the transducer. Also, since we have the electrical mode decoupled from the mechanical ones, the cold damping effect is small and $\frac{Q_a}{Q} \approx 1$. As a result, the thermal noise is dominated by the first term in equation (4.17):

$$S_{I,m} = 4k_B T \,\mathrm{Re}\,(Y_m(\omega)) = 4k_B T \frac{\beta^2 \omega_0^3}{L_2 Q} \frac{1}{\left({\omega_0}^2 - \omega^2\right)^2 + \frac{w^2 w_0^2}{Q^2}} \tag{4.18}$$

The variance of the I_2 due to the thermal noise is given by the integral over the real part of the admittance, which in high Q approximation yields

$$\left\langle I_2^2 \right\rangle = 4k_B T \int \mathrm{Re}(Y_m(\omega)) d\omega = \frac{k_B T}{L_2} \beta^2, \tag{4.19}$$

The equivalent temperature of the modes calculated by comparing the measured energy in the resonant peak S_{II} to the expected thermal energy per Kelvin

$$T_{eq,m} = \frac{L_2}{k_B \beta^2} \int S_{II}(\omega) d\omega. \tag{4.20}$$

Now we can monitor the energy and thus the equivalent temperature of the modes during the operation of MiniGRAIL by using a lock-in amplifier, tuned to the resonance frequency of the mode. But for thirteen modes of MiniGRAIL this would require a use of thirteen amplifiers, which is not realistic. Instead we use an offline software implementation of lock-in amplifier written in Matlab. To exclude the mutual contribution of the neighbouring modes, the data is first filtered with 4-th order Butterworth bandpass filter around the mode frequency and then fed to the lock-in amplifier function. The lock-in time constant was set to 1 s, resulting in 1 Hz integration bandwidth - more than enough for the high Q modes of MiniGRAIL. By repeating the procedure for each mode, we get a full information about the energy stored in the quadrupole modes of the sphere.

The effective temperature of the modes, averaged over one night of the acquisition is shown in the third column of table 4.2

Filtering noisy data

From the average temperature of the modes it is obvious that they are far from thermal noise level and are excited by some external vibrations. Further in this chapter we will try to analyze the cause of this excess noise, but for now we will concentrate on extracting some useful data from our noisy system. If the excitation is stationary there is little we can do. But if the excitation is a periodic or random delta-like signal, which we believe is the case, it acts on the sphere much like a calibration pulse or a gravitational wave. So, we can use standard filtering techniques, developed for resonant detectors [68, 69].

Because of the high mechanical quality factor of the modes, once they are excited it will take hundreds of seconds before the sphere comes to rest, even if the excitation signal is already gone. But because the source of the noise is no more active, the amplitudes of the modes will freely decay to the thermal noise level and any new energy deposited to the sphere will excite the modes again and can be detected. So we need to construct a “peak detection” filter which would emphasize the excitation peaks, but quickly damp the free decay of the sphere after that, effectively lowering

N_{mode}	Frequency, $[Hz]$	$\langle T_{eff} \rangle$, $[K]^a$	$\langle T_{eff}^{filtered} \rangle$, $[K]^b$	$\langle T_{eff}^{100s} \rangle$, $[K]^c$
1	2922.45	18642	3095.6	235.9
2	2930.99	285	66.3	23.8
3	2940.11	334	125.6	103
4	2941.13	290	114.3	88.5
5	2958.57	194893	25035.5	753
6	2968.17	237	111.3	14.6
7	2985.42	16192	5598.2	2828.6
8	3007.75	529	206.8	67.4
9	3016.25	3116	531.2	128.2
10	3024.4	1363	805.3	131.9
11	3030.92	21020	3382.7	576.7
12	3043.33	900	998.2	143.3
13	3057.91	2025	674.1	115.1

a – whole night average

b – whole night average after ZOP filter

c – average of 10 most "quiet" $100\,s$ intervals

Table 4.2**:** Equivalent temperature of the normal modes measured over one night of acquisition.

the Q of the modes. The best solution would be to use an optimal matched filter. Building such a filter would require building a model which describes the spectrum of the normal modes of the sphere [23], which is in case of a complex spectra of real MiniGRAIL setup is hard and computationally extensive task. A simpler, though somewhat suboptimal way is well known for many years [68, 70] and is commonly referred as *zero-order prediction* (ZOP) filter.

Unlike the wideband matched filter, the ZOP filter is applied individually to each mode of the sphere. The ZOP algorithm consists of extracting both quadrature components $x(t)$ and $y(t)$ of the signal at the resonant frequency of the modes (in fact we already did it to estimate the temperature of the modes) and building a difference vector defined as

$$\Delta R_j = \sqrt{(x_j - x_{j-1})^2 + (y_j - y_{j-1})^2}, \tag{4.21}$$

where x_j and y_j are the jth sample of $x(t)$ and $y(t)$ respectively.

The idea of the filter is that for a short lock-in integration time τ_s, much shorter than the decay time of the mode $\tau_0 = \frac{Q}{\pi f_0}$, the variations of the output signal due to the noise are relatively small, while the burst signal will produce a sudden change in the data. The integration time, however has to be high enough not to overdamp the system. The optimal signal-to-noise ratio is achieved when the lock-in time constant is equal to [70]

$$\tau_s^{opt} = \tau_0 \sqrt{(e-1)\frac{S_{wb}}{V_{nb}}\tau_0}, \tag{4.22}$$

where τ_s is the sampling time, τ_0 is a decay time of the mode and $\frac{S_{wb}}{V_{nb}}$ is the ratio between wideband noise spectral density and narrowband noise.

If the condition $\tau_s \ll \tau_0$ is satisfied, the relation between the effective temperature of the mode after filtering and a variance of ΔR is given by the equation [68]

$$\left\langle (\Delta R)^2 \right\rangle = \frac{\beta^2}{L_2} k_B T \frac{\tau_s}{\tau_0} \tag{4.23}$$

As an example, the result of applying the described filter to the $2931\,Hz$ mode data is shown on figure 4.5. After the mode is excited to almost $10^4\,K$, it stays excited for more than $200\,s$. On a filtered data, the energy goes down in a few seconds, and the mode is again at the stationary noise level.

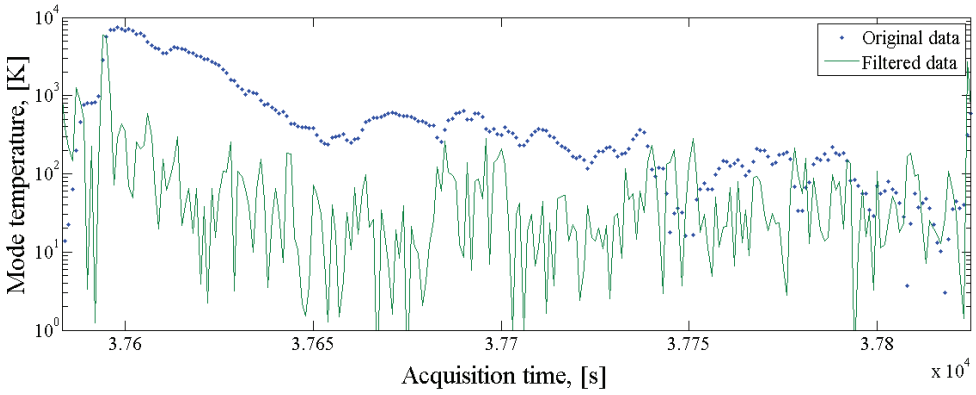

Figure 4.5**:** The "damping" effect of the zero-order prediction filter.

To look for a "quiet" periods of data we can use for sensitivity calculation, we have applied a running average with the window size of $100\,s$ to the filtered data. The window size is a compromise between the high resolution FFT spectra we need for the modes with a $Q \sim 10^5$, and the number of "quiet" spectra we can average. We have selected 10 regions of data with the average temperature below $30\,K$ (see figure 4.6)

The averaged spectra for two working transducers together with the temperature of the modes is shown on figure 4.7.

Note, that the temperature of even the coldest modes is higher than the ones in table 4.2 because the spectra are made from non filtered data.

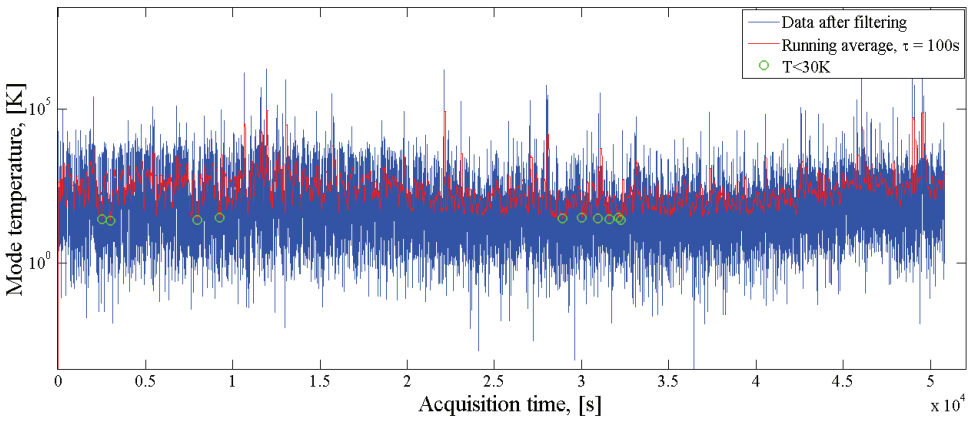

Figure 4.6**:** Equivalent temperature of the "coldest" mode after filtering. Green circles indicate the regions where the average temperature of the mode is below $30\,K$ for at least $100\,s$.

4.2.2 Calibrator's efficiency estimation

Absolute calibrators efficiency

To measure the transfer function of the system we would like to know how much force F^{cal} does the piezo calibrator generate for a given applied voltage V^{cal} - the absolute sensitivity of the calibrators.

If we apply an impulsive force $F_j^{cal} = F_0\delta(t)$ to the calibrator j then the force acting on m quadrupole modes is

$$\mathbf{f}_m = \alpha \mathbf{Y}_m(\phi_j, \theta_j) F_j^{cal} \tag{4.24}$$

The modes amplitude response is Lorentzian:

$$\mathbf{a}_m(\omega) = \frac{1}{M(-\omega^2 + i\frac{\omega\omega_0}{Q} + \omega_0^2)} \mathbf{f}_m, \tag{4.25}$$

where M is the mass of the sphere. The displacement of the sphere surface at the calibrator position due to all five modes is

$$q_j = \alpha \mathbf{Y}'_m \mathbf{a}_m \equiv \alpha^2 \mathbf{Y}_m(\phi_j, \theta_j) \mathbf{Y}'_m(\phi_j, \theta_j) \frac{1}{M(-\omega^2 + i\frac{\omega\omega_0}{Q} + \omega_0^2)} F_j^{cal}, \tag{4.26}$$

which corresponds to the equation of motion for a harmonic oscillator with an effective mass

$$M_{eff} = \frac{M}{\alpha^2 \mathbf{Y}_m(\phi_j, \theta_j) \mathbf{Y}'_m(\phi_j, \theta_j)} \tag{4.27}$$

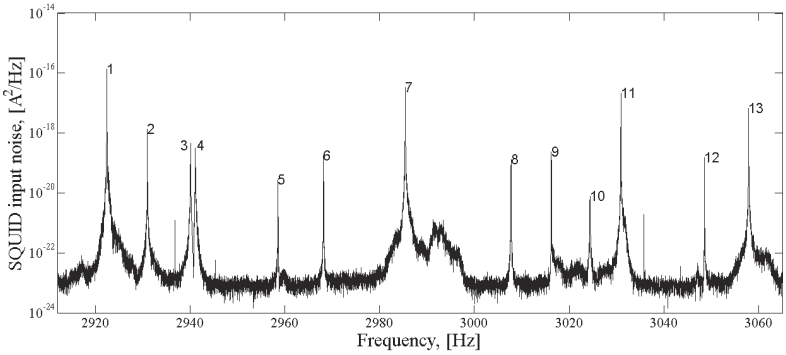

(a) Transducer 4

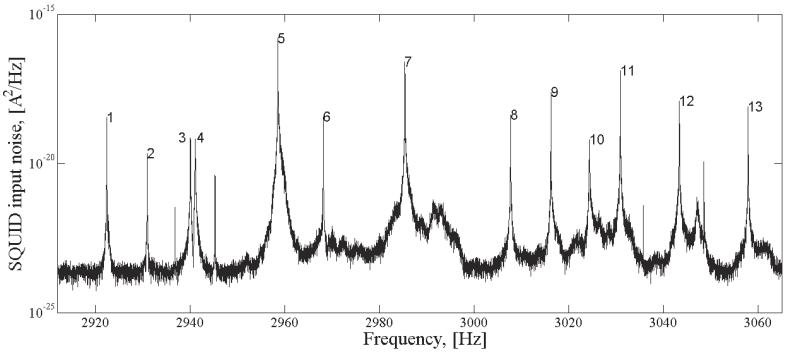

(b) Transducer 6

Mode	Frequency, [Hz]	Temperature, [K]
1	2922.45	5783.0594
2	2930.99	93.4974
3	2940.11	169.977
4	2941.13	235.9964
5	2958.57	15845.3661
6	2968.17	81.3254
7	2985.42	6607.2316
8	3007.75	146.6755
9	3016.25	981.8123
10	3024.4	646.4108
11	3030.92	8545.8511
12	3043.33	342.4096
13	3057.91	1129.668

(c) Effective temperature of the modes

Figure 4.7**:** The averaged spectra for Transducer 4 (a) and Transducer 6 (b). The averaging is done over 10 most "quiet" regions of data. (c) – the corresponding effective temperature of the modes.

For miniGRAIL $\alpha = 2.9$ and $\mathbf{Y}_m(\phi_j, \theta_j)\mathbf{Y}'_m(\phi_j, \theta_j) = 5/4\pi \approx 0.398$ resulting an effective mass, associated with the normal modes of the sphere to be $M_{eff} \approx 0.3M$

The energy transferred from the calibrator J to the quadrupole modes of the sphere is

$$E = \frac{(F_j^{cal})^2}{2M_{eff}} \tag{4.28}$$

Now we can excite each calibrator with a known voltage and, since we have also done the energy calibration in the previous section, measure the total energy stored in the normal modes of the sphere. From equation (4.28) we can calculate the generated force F_j^{cal} and estimate the efficiency of each calibrator.

The calculated efficiency is almost equal for all calibrators and lies in the order of $1 \times 10^{-2}\, N/V$. A rough estimate of a room temperature calibrator efficiency using a simple model of a mass-loaded spring gives $\sim 10^{-1}\, N/V$. Given that typically piezo crystal performance degrades at low temperatures by a factor of $4 - 5$, we found the calculated results to be reasonable.

Relative calibrators efficiency

The calibration procedure described above relies on the accuracy of the energy calibration of the modes, which depends on the transducer-mode coupling. We have performed another approach that allows to estimate the relative efficiency of the calibrators.

We assume that the linear combination of calibration excitations that does not produce any quadrupole excitation because is highly symmetric and thus should only excite the monopole mode of the sphere. If we have a set of J equivalent calibrators, then the combination of calibrators forces that excite only the monopole mode are given by

$$\mathbf{F}_j = \mathbf{B}_{mj}^{-1}\mathbf{F0}_m, \tag{4.29}$$

where $\mathbf{F0}_m = [1, 0, 0, 0, 0, 0]$ is the modes force vector, where the first unity amplitude represents the monopole mode and 5 zeros are the amplitude of quadrupole modes forces. Here and in the rest of this chapter we use 6×6 $\mathbf{B}$ matrix, which includes the monopole mode (see section 1.2.4 in chapter 1). Also we omitted the radial eigenfunction coefficient α, as it does not influence the result. Now if we apply the calculated $\mathbf{F}_j$ vector to the real calibrators transfer functions and multiply it by a pattern matrix $\mathbf{B}_{mj}$ the result will be non-zero forces, acting on quadrupole modes. Our task is then to find such a vector $\mathbf{F}'_j = \mathbf{F}_j\mathbf{e}_j$ for which the resulting modes excitation is $\mathbf{F0}_m$. Vector $\mathbf{e}_j$ is the inverse of relative calibrators efficiency ϵ_j. The result of such calculation for both working transducers is shown on figure 4.8. Calibrator 7 transfer function is given for comparison. The amplitudes of the quadrupole modes are clearly reduced by at least one order of magnitude.

We found that fitted efficiency comes in reasonable agreement between two transducers and is also consistent with rough room temperature estimation in section 4.2.3

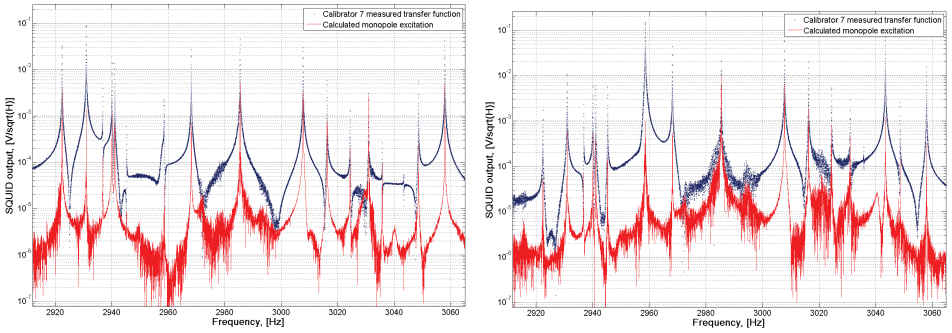

(a) Transducer 4 (b) Transducer 6

Figure 4.8**:** Monopole mode excitation compared to the Calibrator 7 transfer function

	Cal1	Cal2	Cal3	Cal4	Cal5	Cal6
Energy calibration	0.7861	0.8537	1.0	0.8226	0.9016	0.8921
Room temp Calibrator7 fit	0.63	0.60	1.0	0.60	0.80	0.61
Monopole mode fit Tr4	0.6043	0.5630	0.9660	0.6952	0.5657	0.5273
Monopole mode fit Tr6	0.5955	0.5692	1.1319	0.6304	0.5269	0.5017
Ratio Tr4/Tr6	0.9855	1.0110	1.1717	0.9068	0.9313	0.9514

Table 4.3**:** Calibrators efficiency ϵ calculated from fitting transfer functions of six calibrators to monopole excitation

(table 4.3). We have also noticed that the calibrators efficiency obtained from the energy calibration is more uniform than the one from the monopole mode fitting. We believe this is because the fitting procedure "automatically" compensates the non-ideality of the MiniGRAIL sphere which becomes more obvious further in this chapter.

4.2.3 Direction reconstruction

In this section we show the results of the direction reconstruction algorithms, described in chapter 1, applied to the real data of MiniGRAIL. We use the Calibrators 1-6 to measure the full transfer function of the system and a signal from Calibrator 7 simulating the candidate GW signal, coming from unknown direction. The direction reconstruction procedure is similar to calibrators efficiency estimation algorithm. If $Fq_7(\omega)$ is the force that Calibrator 7 applies to the sphere, the forces acting on the normal modes are

$$\mathbf{Fa}_m(w) = \epsilon_7 \mathbf{Y}_m(\phi_7, \theta_7) F q_7(\omega), \tag{4.30}$$

where (ϕ_7, θ_7) is the position of Calibrator 7 which is not known and ϵ_7 is the efficiency of the Calibrator 7, which is just a scaling factor. The forces $\mathbf{Fq}_{1..6}(\omega)$ that Calibrators 1-6 have to apply to produce the same modes forces are given by

$$\mathbf{Fq}_j(\omega) = \mathbf{e}_j\mathbf{B}_{mj}^{-1}\mathbf{Fa}_7(\omega) = \epsilon_7\mathbf{e}_j\mathbf{B}_{mj}^{-1}\mathbf{Y}_m(\phi_7,\theta_7)Fq_7(\omega) \equiv \lambda\mathbf{Y}_m(\phi_7,\theta_7)Fq_7(\omega), \tag{4.31}$$

where $\lambda = \epsilon_7\mathbf{e}_j\mathbf{B}_{mj}^{-1}$ is a constant vector because $\mathbf{B}_{mj}$ depends only on Calibrators 1-6 positions, which is known and fixed, ϵ_7 and $\mathbf{e}_j$ we have calculated by fitting the monopole mode in section 4.2.2.
Now we can vary ϕ_7 and θ_7 until the error between measured $Fq_7^{meas}(w)$ and calculated $Fq_7^{calc}(w)$ force amplitudes is minimized. We calculate the fitting error as

$$\xi = \sum_{\omega} |\log(\frac{q_7^{meas}(\omega)}{q_7^{calc}(\omega)})|. \tag{4.32}$$

Here, we use a base 10 logarithm of the amplitudes relation to equalize the weight of the fitting error between the resonances and antiresonances.

Room temperature results

We have performed the first tests on the sphere with transducers at room temperature in normal atmospheric pressure. Because the transducers are damped by air, the quality factor of the modes was very low. However we could verify that all calibrators are working properly before closing the cryostat. The measurements were done with a transducer mounted on transducer position 4. Transducer was enclosed in a small vacuum cap and charged to $142\,V$. The transfer functions were acquired by frequency sweeping the excitation signal and measuring the response with a lock-in amplifier.

Because of the low quality factor of the modes we did not actually fit the Calibrator 7 transfer function. Instead we measured ϕ_7, θ_7 and used the calculated $\mathbf{Y}_m(\phi_7,\theta_7)$ to check the calibrators. In fact, we have found that 2 calibrators had an inverted polarity and fixed them before closing the Dewar. We have also roughly estimated the relative efficiency of the calibrators. These are the room temperature values listed in table 4.3.

Low temperature results

Cryogenic calibration was done at a temperature of $1\,K$. To save time we used an impulse calibration instead of frequency sweeping the calibration signal.

We have tried two fitting approaches which we will further refer as “Fit1” and “Fit2”.

With a “Fit1” we used the equation (4.31) and fitted values of ϕ_7 and θ_7 . A result of the fitting is shown on figure 4.10 in red. We found that the agreement between the fitted curve and the measured data was reasonably good. The calculated Calibrator 7 position was consistent between two acquisition channels, but was more than 20 % off the measured values.

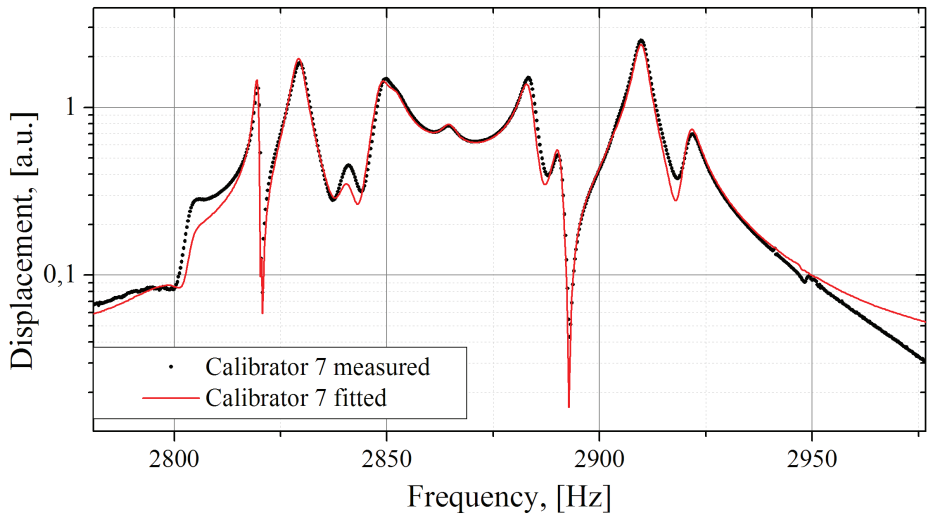

Figure 4.9**:** Room temperature fit of Calibrator 7 transfer function.

In another approach("Fit2") we have tried to find such a linear combination $\mathbf{a}_j$ of Calibrators 1-6 transfer functions that produces the best fit of the Calibrator 7 transfer function. The major difference of this approach is that $\mathbf{Fa}_j$ does not necessarily correspond to a real excitation applied to the sphere surface and in principle should not necessarily produce a physically meaningful result. On the other hand if the shape of the spherical harmonics of MiniGRAIL deviates from the theoretical shape for the ideal sphere we can still fit the data. The result of the second fit is shown on figure 4.10 in green. The fit is clearly better than the first one. We can still try to calculate Calibrator 7 position by converting the vector $\mathbf{a}_j$ to a mode channels $\mathbf{g}_m$ and calculating a detector response matrix. The eigenvectors of the response matrix show the orientation of the deformation ellipsoid, as described in section 1.2.1. Surprisingly, the values of ϕ_7 and θ_7 obtained from "Fit2" were much closer to the measured ones. The shape of the deformation ellipsoid, however was very distorted. For an ideal sphere the maximum radial deformation is at the location of the calibration impulse, and two radial deformations in the orthogonal directions have an opposite sign and half amplitude. The calculated deformation ellipsoid is very asymmetric - the deformations in orthogonal directions are not equal. However, their sum is equal to the main axis deformation, so the volume is preserved. We believe that the reason of such deviation is either in a structural imperfection of the sphere, like a non uniform density distribution, or in a non uniform stress induced by the sphere suspension. We also noticed that the frequency distribution of the normal modes of the uncoupled sphere is different from the theoretical ones calculated in [19]. As a simple solution we have tried to introduce an amplitude and angular distortion to the

	Measured	Fit1		Fit2	
		Ch4	Ch6	Ch4	Ch6
ϕ, $[deg]$	33	40.8	41.6	36.8	35.8
θ, $[deg]$	51	61.6	61.1	48.3	48.5

Table 4.4**:** Calculated Calibrator 7 position compared to the measured one. Fit1 is made by using an elastic model of an ideal sphere. Fit2 is done by fitting Calibrator 7 with a linear combination of Calibrators 1-6 transfer functions.

spherical harmonics in equation (1.4), but the results were not consistent anymore between the acquisition channels. The results of both fits are summarized in table 4.4

Effect of calibration signal jitter

To increase the signal to noise ratio, the transfer function of each calibrator was measured for 20 times and then averaged. During the averaging we noticed that the relative amplitudes of the peaks are changing. We have discovered that the problem was in the time stability of the calibration pulse. Originally we used a software triggered calibration - a LabView program starts the acquisition and after a time delay sends a command to the function generator to generate a calibration pulse.
Let's consider a frequency domain representation of a calibration signal. If we apply a discrete Fourier transform defined as

$$X_k = \sum_{n=0}^{N-1} x_n e^{-\frac{2\pi i}{N} kn} \qquad k = 0, \ldots, N-1 \tag{4.33}$$

to the delta-like calibration signal with amplitude A and at sample index j, the corresponding frequency domain signal will be

$$X_k = A e^{-\frac{2\pi i}{N} kj} \qquad k = 0, \ldots, N-1, \tag{4.34}$$

The amplitude and phase of the calibration signal in frequency domain are

$$\begin{aligned} R_k &= |X_k| = A \\ \varphi_k &= \arctan\left(\frac{\mathrm{Im}(X_k)}{\mathrm{Re}(X_k)}\right) = \arctan\left(\frac{\sin(\frac{2\pi kj}{N})}{\cos(\frac{2\pi kj}{N})}\right) = \frac{2\pi kj}{N} \end{aligned} \tag{4.35}$$

The amplitude R_k is constant in frequency, just as we want for a calibration signal, but the phase is changing by 2π radians every $kj = N$. If the time and thus the index j of calibration pulse is not stable, the slope of the phase will vary from acquisition to acquisition.

To overcome this effect we have set up a hardware double triggered calibration - first trigger starts the ADC card acquisition and the second one triggers the function generator to send a calibration pulse. The time delay between two trigger signals is

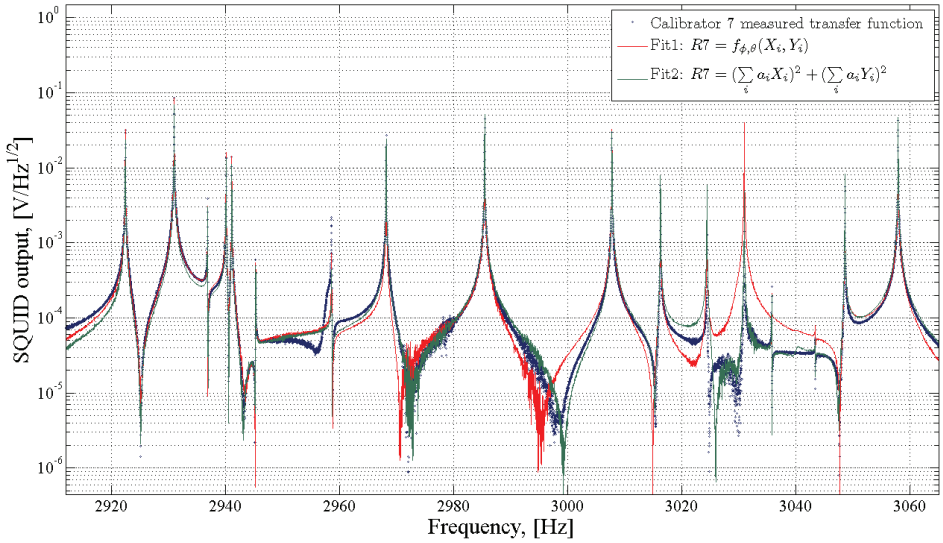

(a) Transducer 4

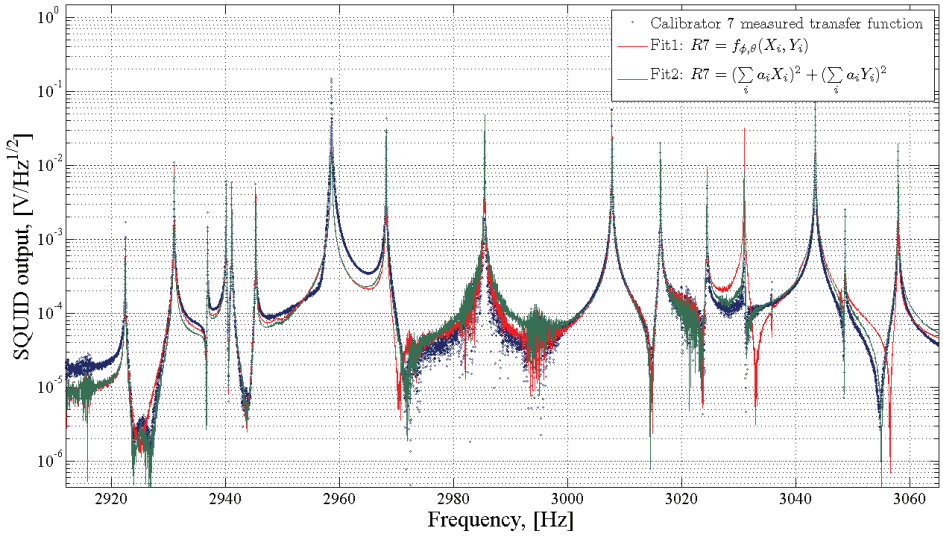

(b) Transducer 6

Figure 4.10**:** Calibrator 7 transfer function fit

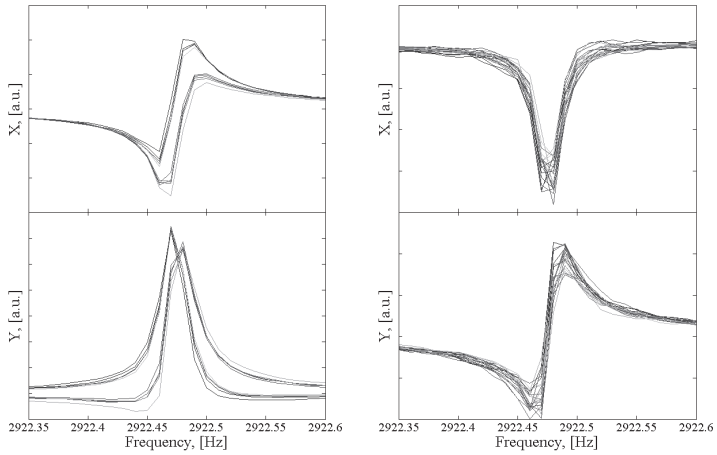

Figure 4.11**:** Two quadrature components of a 2922.45 Hz mode transfer function acquired multiple times with software(a) and hardware(b) triggering. Software triggering introduces a phase jitter making averaging impossible.

also done with hardware timer. To further improve the stability we are also acquiring the calibration signal and subtracting its phase from the phase of the measured transfer function. The real and imaginary parts of the 2922.45 Hz mode transfer function, measured with software and hardware triggering is shown on figure 4.11. On figure 4.11(a) the phase is clearly bistable, corresponding to values of j varying by 1.

4.3 Strain sensitivity

From chapter 1 we recall that the force induced by an incident gravitational wave to the sphere can be decomposed in five quadrupole components F_m:

$$F_m(t) = \frac{1}{2} R\chi M \ddot{h}_m(t), \tag{4.36}$$

or in frequency domain[28]:

$$F_m(\omega) = \frac{1}{2}\omega^2 M\chi R\ h_m(\omega) = \frac{1}{2}\omega^2 M\chi R \mathbf{T}_V \begin{bmatrix} h_+(\omega) \\ h_\times(\omega) \end{bmatrix}, \tag{4.37}$$

where R, M are the sphere radius and mass, $\chi = 0.327$ is an effective length and h_m are gravitational wave spherical amplitudes, related to two polarizations states of a gravitational wave by means of conversion matrix $\mathbf{T}_V$.

What we measure at the output of the detector is not the force, but the current density at the input coil of the SQUID amplifier. The five components of the force $F_m(\omega)$ are converted to six current outputs I_j by a rectangular 6×5 transfer matrix $\mathbf{Tf}_{jm}$. So to go back from measured currents to forces we need to inverse the **Tf** matrix. In case of at least 5 (or even 4 with some limitations[32]) transducers the system is fully determined so we can invert the transfer matrix and construct statistically independent mode channels to perform a coherent data analysis as described in chapter 1.

In our case, we only have 2 working transducers. Of course it is not possible to reconstruct 5 quadrupole amplitudes by measuring only at 2 positions of the sphere, so the system is underdetermined. In principle, since the modes are non-degenerate, we can see all the quadrupole modes individually in each transducer output spectrum (see figure 4.7). Since we have measured the transducer-mode coupling for each mode, we can calculate the amplitudes of the modes at the transducer position and thus do the direction estimation. In practice, however, we were not able to clearly identify the modes in the MiniGRAIL spectra.

What we can still do is to combine the transfer functions we have measured from 6 calibrators, to simulate the gravitational wave excitation of the sphere from any direction, defined by two polar angles β and γ:

$$Tf(\beta,\gamma) = \left(\mathbf{Tv}(\alpha,\beta,\gamma)\begin{bmatrix} h_+(\omega) \\ h_\times(\omega) \end{bmatrix}\right)' \mathbf{B}(\beta_c,\gamma_c)\mathbf{Tf}_c(\omega), \tag{4.38}$$

where α is the polarization angle of gravitational wave which is not known beforehand. So for simplicity we set $\alpha \equiv 0$ and build the sky sensitivity map for every transducer by varying β and γ

$$S_{hh_j}(\omega,\beta,\gamma) = \frac{S_{I_j}(\omega)}{Tf(\omega,\beta,\gamma)}, \tag{4.39}$$

where S_{I_j} is the noise current power spectral density at the SQUID input. Close to the resonance the output noise is limited by the detector noise, and the outputs of the transducers are correlated. For that reason we can not sum the signal-to-noise ratios of the transducers. Instead we took the minimum of two transducers sensitivity, which is correct at the resonance, but a factor $\sqrt{N_{tr}}$ suboptimal at the regions where the transducers noise is not correlated.

The strain sensitivity curves from an optimal direction for "plus" and "cross" polarized gravitational wave are shown on figure 4.12. As expected from the high equivalent temperature of the modes, it is quite far from $4.2\,K$ thermally limited sensitivity(dashed line). The $4\,K$ sensitivity plot is made with exactly the same system properties, but with the energy of the modes set to thermal. The $20\,mK$ plot is done by setting the equivalent temperature of the modes to 20mK and increasing the coupling of the modes by a factor of 3 to match the design value of transducers bias field. Around the resonant peaks the best sensitivity of two transducers is taken, same as for measured curve. In the uncorrelated parts of the spectra, dominated by the SQUID additive noise, we took the sum of SNR of two transducers, resulting an

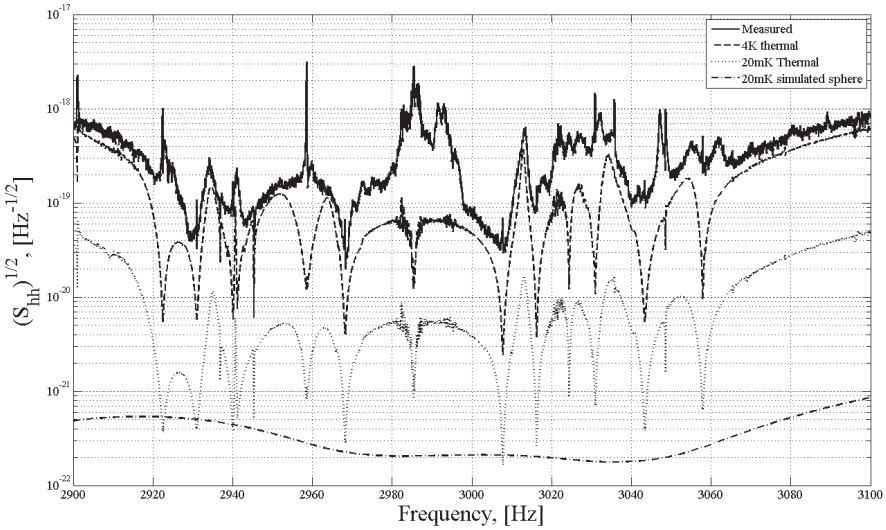

(a) h_+, ($\beta = 50^o\, \gamma = 180^o$)

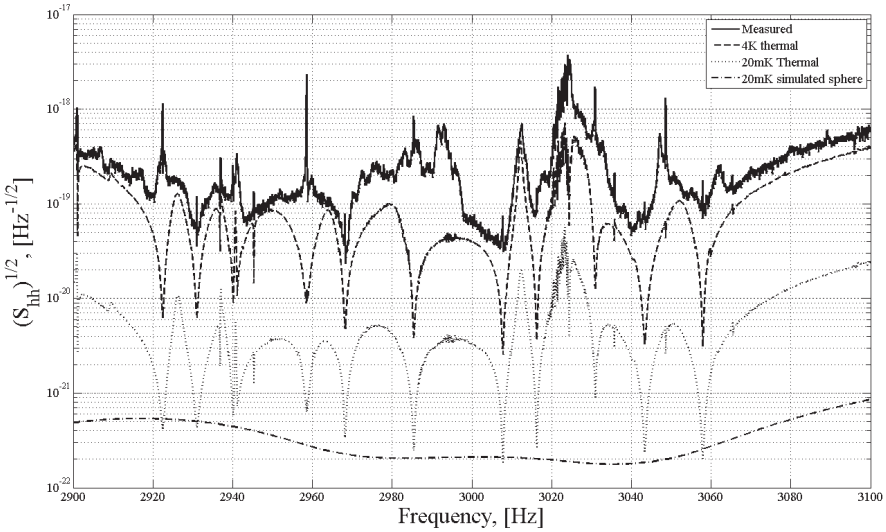

(b) $h_\times$, ($\beta = 55^o\, \gamma = 120^o$)

Figure 4.12**:** Best strain sensitivity from two transducers combined for "plus" (a) and "cross" (b) polarized gravitational wave. The sensitivity is calculated for best SNR direction for each polarization. The $4\,K$ and $20\,mK$ thermal strain sensitivities are made by generating a thermally limited noise spectra and 3 times increased coupling for $20mK$ data. Simulated data is taken from [32]

improved wideband sensitivity. The simulated curve is made by building a numeric model of the sphere with transducers and read-out circuit[32][1].

For both polarization states, the measured sensitivity curves were very similar with a best peak strain sensitivity of $3 \times 10^{-20}\, Hz^{-1/2}$ and a strain sensitivity of $1 \times 10^{-19}\, Hz^{-1/2}$ over a bandwidth of $42\, Hz$. That is about factor 2 worse than the 5 K nearly thermally limited sensitivity reported in [25]. For the $4.2\, K$ thermally limited noise spectra and current system parameters we would reach a peak strain sensitivity of $2.6 \times 10^{-21}\, Hz^{-1/2}$ even with only 2 working transducers. The peak sensitivity level for current configuration and thermodynamic temperature of the sphere of $20\, mK$ is about 2×10^{-22} Hz$^{-1/2}$

In order to compare the sensitivity to other detectors we calculate the integral sensitivity parameter - the minimal detectable Fourier amplitude of gravitational wave burst which is defined as

$$H_0(\omega, \beta, \gamma) = \frac{1}{\sqrt{SNR}} = \frac{1}{\left(\int \frac{1}{S_{hh}(\omega,\beta,\gamma)} \frac{d\omega}{2\pi} \right)^{1/2}} \tag{4.40}$$

The measured sensitivity curve on figure 4.12 corresponds to a gravitational wave burst with a Fourier amplitude $H_0 = 8 \times 10^{-21}$ or an energy of $T_N = 2.3$ K. A calculated 20 mK sensitivity would yield $H_0 = 1 \times 10^{-22}$ and the pulse detection noise temperature[2] $T_N = 4.5 \times 10^{-4}$ K, which is about 1.5 times better than the one of Auriga [72], which is the most sensitive resonant detector at the moment.

A directional dependence of the integral sensitivity for both GW polarizations is shown on figure 4.13(a,b). The third plot on figure 4.13(c) shows the strain sensitivity to the calibration pulse. While having obviously no meaning in terms of gravitational waves sensitivity, it is given to compare the calculated sky sensitivity with a simple model described in section 4.1. The H_0 plot on figure 4.13 is somewhat different from the one on figure 4.1(c) because of influence of the modes coupling to the transducer, but it is clearly more uniform than the sensitivity plot with the degenerate modes on figure 4.1(b). It is also a good illustration that for a spherical detector a mechanical excitation of the sphere is not fully identical to gravitational waves excitation. We have discussed that in section 1.2.4 of chapter 1.

4.4 Conclusions

For the first time we have cooled MiniGRAIL down in a full 6-transducer configuration, capable of omnidirectional detection. During the run we have faced two serious

[1] A simulated 20 mK sensitivity plot on figure 4.12 is much smoother than the one estimated by us for two reasons. First, non working transducers do not contribute in sensitivity, instead they are extracting the energy from the system at their resonant frequency. They appear as antiresonances on the transfer function and as sharp dips on the sensitivity plot. Second, the value of the wideband SQUID noise in [32] is calculated by using a Clarke-Teshe model[26] and appears to be much lower than the noise achievable with a practical SQUID amplifier we use.

[2] The pulse detection noise temperature, T_N, is defined by $E = k_B T_N$, where E is the energy deposited to the sphere by a gravitational wave resulting in $SNR = 1$ [71]

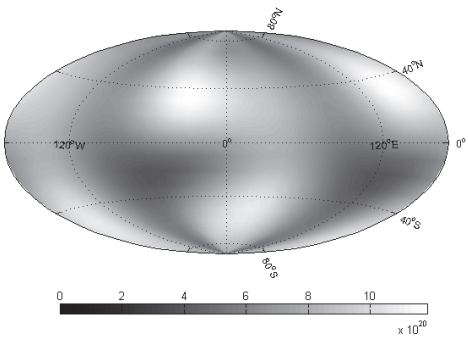

(a) h_+ polarized GW. $H_0 = 8.4 \times 10^{21}$

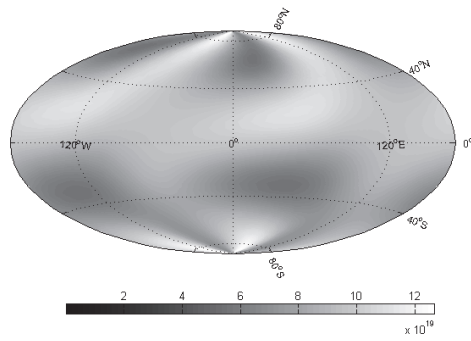

(b) $h_\times$ polarized GW. $H_0 = 7.9 \times 10^{21}$

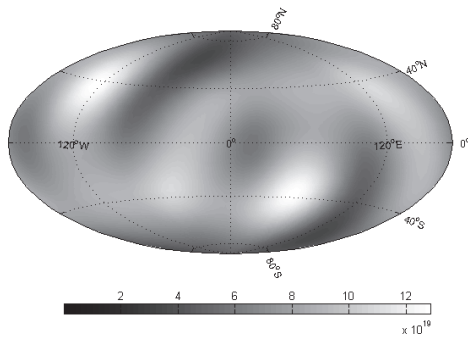

(c) Calibration excitation

Figure 4.13**:** The minimal detectable Fourier burst amplitude versus the direction for two polarizations of gravitational wave and calibration excitation

problems: Transducers failure and excess vibrational noise. We could measure the capacitance and charge transducers through a bias line up to the temperature of about $40\,K$, but failed to bias the transducers at $4.2\,K$. We have discovered that the reason was that the reed switches we have used contained exchange gas, which was not clearly indicated in a datasheet. Exchange gas would condense and freeze on the electrodes at low temperatures and block them. We could heat up the switches by sending a short high current pulse to the coil of the switch and restore the operation, but that would disturb and warm up MiniGRAIL as well. Another problem we have discovered is that the long and very soft shielded wires we used to connect the transducers to the charging lines (see figure 1.10) were attracted by the electrode's electric field and were touching the electrodes with the shield, shorting them to ground. These issues can be easily fixed before the next cool down. After finishing the current run and opening the cryostat we have discovered that all the transducers were still working.

Concerning the second problem, since we have already reached a thermal noise level in previous runs, there is obviously no fundamental problem with the suspension of the sphere. Before this run we have changed the old copper "jelly-fish" thermal links with new thicker ones to improve their thermal conductance at the cost of damping. Also since it is the first time we have cooled down MiniGRAIL with all 6 transducers and 7 calibrators, the amount of wires going to the sphere and the last mass have increased a lot. For the next cool down we are planning to add an extra vibration insulation stage for the cables, suspended from mixing chamber or $50\,mK$ plate.

The two problems, described above resulted that only two out of six transducers were operational and far from thermal noise. The data analysis pipeline of MiniGRAIL is based on the fact that a spherical detector is a multichannel detector. But since the transducers outputs are correlated around the resonance, we need to convert them to uncorrelated mode channels, which correspond to five spherical amplitudes of a gravitational wave. This means that to build a fully determined system we would need to have at least 5 working transducers. For the 2 transducers configuration we had in this run, the system is underdetermined and the data analysis capability is limited. However, all the calibration and direction reconstruction routines we have developed during this run are made as general as possible and do not depend on the number of transducers. This should allow us to make a calibration and estimate the strain sensitivity of MiniGRAIL within a few days in any future run. As for the current run, we were able to determine the "unknown" position of Calibrator 7 with the accuracy of about $10 - 20\%$, depending on the fitting algorithm. A more precise fitting, constrained to the elastic properties of the sphere gives a higher fitting error, clearly indicating that the behaviour of MiniGRAIL sphere is different from the model of an ideal sphere. the deformation ellipsoid shape, calculated from the best fit is asymmetric. While the fitted results are still reasonably good, we do not have a clear understanding of the reasons of inconsistency and need to perform more tests with more calibration impulse directions, to verify the consistency of the algorithms. Fortunately these tests can also be done at room temperature.

While the sensitivity was heavily affected by the vibrational noise, we have measured a best peak strain sensitivity of $3 \times 10^{-20}\,Hz^{-1/2}$ and a strain sensitivity of $1 \times 10^{-19}\,Hz^{-1/2}$ over a bandwidth of $42\,Hz$, which is factor 2 worse then the $5\,K$ nearly thermally limited sensitivity reported in [25]. This corresponds to a gravitational wave burst with a Fourier amplitude $H_0 = 8 \times 10^{-21}$ or an energy of $T_N = 2.3$ K.

The calculations show, that for the $4.2\,K$ thermally limited noise spectra and current system parameters we would reach a peak strain sensitivity of $2.6 \times 10^{-21}\,Hz^{-1/2}$ even with only 2 working transducers.

The ultimate sensitivity level for current configuration and thermodynamic temperature of the sphere of $20\,mK$ is about $2 \times 10^{-22}\,Hz^{-1/2}$, yielding $H_0 = 1 \times 10^{-22}$ and $T_N = 4.5 \times 10^{-4}$ K. This is about 1.5 times better than H_0 of Auriga [72]- the most sensitive resonant detector at the moment.

Unlike the mechanical part of MiniGRAIL, the electrical read-out part gave no problems. With improved magnetic shielding, redesigned 2-stage SQUIDs and a "cold damping" network, adapted for differential SQUID electronics, the acquisition system

was stable and robust.

Currently, we are planning to fix the issues mentioned above and perform a new run with hopefully all 6 transducers working before the end of 2011. After that the future of MiniGRAIL project is still unclear.